A Novel Transformation Electromagnetics Technique Based on the Schwarz-Christoffel Theorem

M. Salucci, A. Polo, and G. Oliveri

Abstract

This work presents an innovative technique for designing metamaterial lenses covering conformal phased arrays installed on arbitrarily-shaped hosting structures. More in detail, the design of such field manipulation devices is formulated within the transformation electromagnetics (*TE*) paradigm, and its solution is based on the exploitation of the Schwarz-Christoffel theorem in order to perform the spatial transformation between arbitrary doubly-connected “virtual” and “physical” regions. Some numerical results dealing with different settings of the transformation regions are shown to verify the effectiveness as well as the flexibility of the developed technique.

1 Definitions

- Maximum directivity

$$D_{max}(\theta,\varphi) = \frac{4\pi \max_{(\theta,\varphi)}\{|E(\theta,\varphi)|^2\}}{\int_0^{2\pi}\int_0^{\pi} |E(\theta,\varphi)|^2 \sin(\theta) d\theta d\varphi} \tag{1}$$

- Sidelobe level (SLL)

$$SLL = 20 \times log_{10}\left(\frac{\max\{F(\theta,\varphi)\}}{\max\{E(\theta,\varphi)\}}\right) \tag{2}$$

where $F(\theta,\varphi)$ is the $E(\theta,\varphi)$ secondary lobes

- Maximum lens permittivity

$$\max\{\underline{\underline{\varepsilon}}\} = \max_{\underline{r}\in\Omega}\{\varepsilon_{pq}(\underline{r});\ p,q\ \in\{1,2,3\}\} \tag{3}$$

- Minimum lens permittivity

$$\min\{\underline{\underline{\varepsilon}}\} = \min_{\underline{r}\in\Omega}\{\varepsilon_{pq}(\underline{r});\ p,q\ \in\{1,2,3\}\} \tag{4}$$

- Average fractional anisotropy

$$\alpha_F = \frac{1}{area(\Omega)}\int_{\underline{r}\in\Omega}\sqrt{\frac{3\sum_{i=1}^{3}[\sigma_i(\underline{r})-\sigma_{ave}(\underline{r})]^2}{2\sum_{i=1}^{3}[\sigma_i(\underline{r})]^2}}d\underline{r} \tag{5}$$

- Average relative anisotropy

$$\alpha_R = \frac{1}{area(\Omega)}\int_{\underline{r}\in\Omega}\sqrt{\frac{\sum_{i=1}^{3}[\sigma_i(\underline{r})-\sigma_{ave}(\underline{r})]^2}{3\sigma_{ave}(\underline{r})}}d\underline{r} \tag{6}$$

where

  - $\sigma_i(\underline{r}),\ i=1,...,3$ are the eigenvalues of the permittivity tensor $\underline{\underline{\varepsilon}}(\underline{r})$;
  - $\sigma_{ave}(\underline{r}) = \frac{\sum_{i=1}^{3}\sigma_i(\underline{r})}{3}$ is the average of the eigenvalues;
  - Ω is the space region that defines the lens

- Far-Field Matching Error

$$\xi = \frac{\sum_{u=1}^{U}\sum_{v=1,\ (u,v)\notin\Omega}^{V}|E_{est}(\theta_u,\varphi_v)-E_{ref}(\theta_u,\varphi_v)|^2}{\sum_{u=1}^{U}\sum_{v=1,\ (u,v)\notin\Omega}^{V}|E_{ref}(\theta_u,\varphi_v)|^2} \tag{7}$$

- Near-Field Matching Error

$$\chi = \frac{\sum_{u=1}^{U}\sum_{v=1,\ (u,v)\notin\Omega}^{V}|E_{est}(x_u,y_v)-E_{ref}(x_u,y_v)|^2}{\sum_{u=1}^{U}\sum_{v=1,\ (u,v)\notin\Omega}^{V}|E_{ref}(x_u,y_v)|^2} \tag{8}$$

2 Numerical Results

The target of this analysis is to consider different geometries in order to evaluate the advantages and disadvantages of the Schwarz-Christoffel transformation. For every geometry, the following key performance indicators will be reported:

- Maximum Directivity [dB] (1)
- Side-Lobe Level (SLL) [dB] (2)
- Half-Power Beamwidth (HPBW) [deg]
- First-Null Beamwidth (FNBW) [deg]
- Field Matching Error in far-field ξ (7) and near-field χ (8)

2.1 Parameters

- Array:
  - Radius of circular array: $r_{array} = 5.25\ [\lambda]$
  - Elements spacing: $d = 0.5\ [\lambda]$
- Virtual Region
  - Virtual ground plane radius: $r_{virt-gnd} = 5\ [\lambda]$
  - Distance from the ground plane: $\delta = r_{array} - r_{virt-gnd} = \frac{\lambda}{4}$
  - Virtual permittivity: $\varepsilon = 1$
  - Virtual permeability: $\mu = 1$
- SCTO parameters
  - Error tolerance: 10^{-10}
  - Number of Gauss-Jacobi points (nodes): 6
  - Discretization in virtual grid (outer boundary): $\Delta = 0.1\ [\lambda]$
  - Control point angle for the compensation angle computation: $\varphi_{cp} = 90$ [deg]
- Simulation Environment
  - Working frequency: $f_w = 300\ [MHz]$
  - Simulation region: $\begin{cases} x \in [-20,\ 20]\ [\lambda] \\ y \in [-20,\ 20]\ [\lambda] \end{cases}$
  - Near-Field computation: $\begin{cases} x \in [-20,\ 20]\ [\lambda] \\ y \in [-20,\ 20]\ [\lambda] \end{cases}$
  - Far-Field computation: $\begin{cases} \theta = \frac{\pi}{2}\ [rad] \\ \varphi \in [0,\ \pi]\ [rad] \end{cases}$
  - Mesh settings
    - Size: $size_{mesh} \in [5 \times 10^{-4}, 0.2]$
    - Maximum growth rate: 1.3
    - Curvature factor: 0.3
    - Narrow region resolution: 1
  - Simulation region layer thickness: 1

2.1.1 Results - Geometry 1 - Internal Square

Parameters

- Number of elements: $N = 16$
- Physical Region
  - External radius: $L_{ext} = 14$ $[\lambda]$
  - External Lens boundary : $\partial\Omega_{ext} = \left\{(x, y) \in \mathbb{R} \mid \sqrt{x^2 + y^2} = L_{ext}\right\}$ $[\lambda]$
  - Internal Lens boundary: $\partial\Omega_{int} = \{(5; 5),\ (-5; 5);\ (-5; -5),\ (5, -5)\}$ $[\lambda]$
  - Number of points defining the external boundary: $n_{ext} = 30$
  - Number of points defining the internal boundary: $n_{int} = 4$

Results

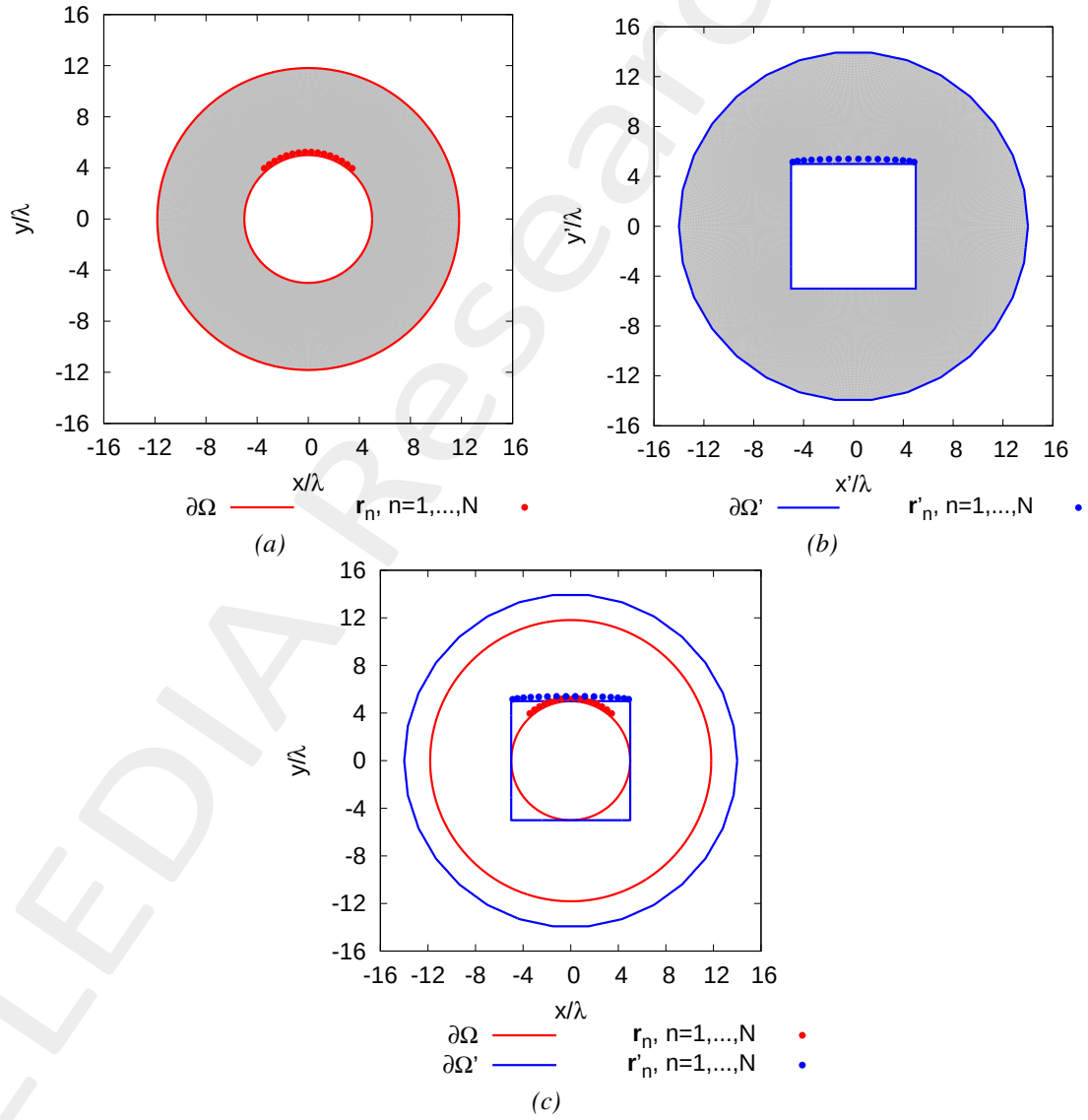

Figure 1: *(a)* Virtual, *(b)* Physical geometries and *(c)* the comparison

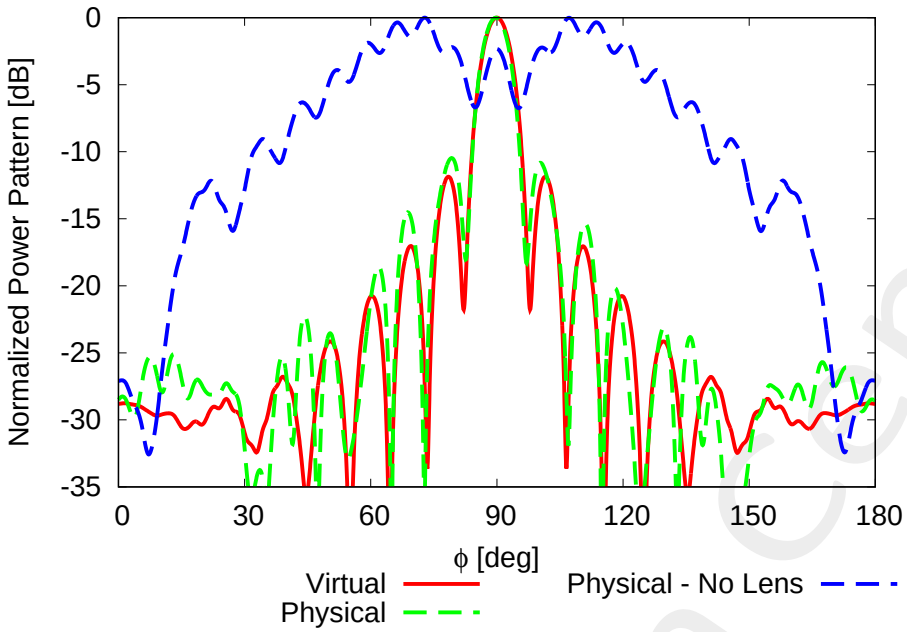

Figure 2: Far-Field Pattern for $\theta = 90$ [deg] and $\varphi \in [0, 180]$ [deg]

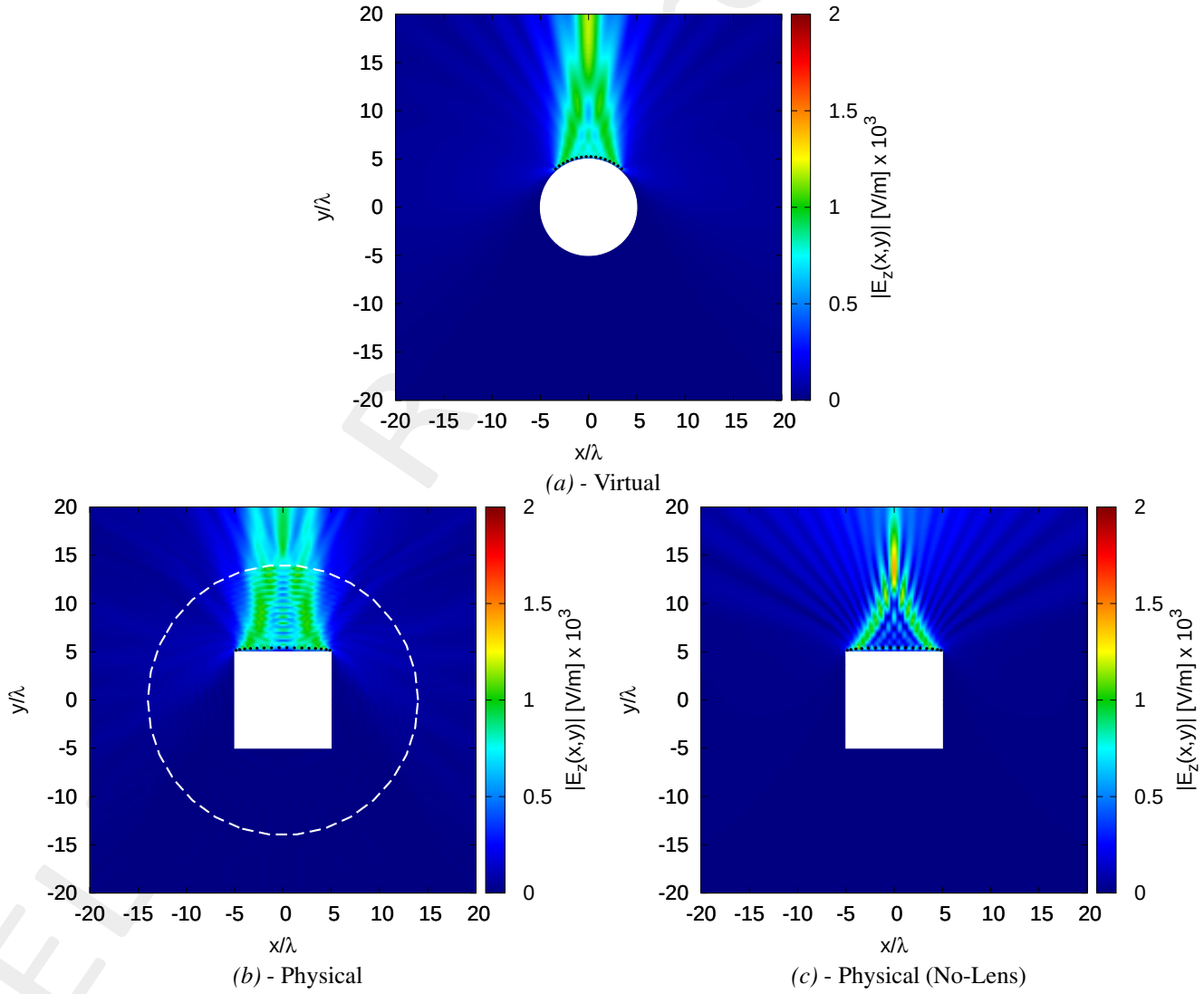

Figure 3: Near-Field pattern in the *(a)* virtual, *(b)* physical and *(c)* no-lens

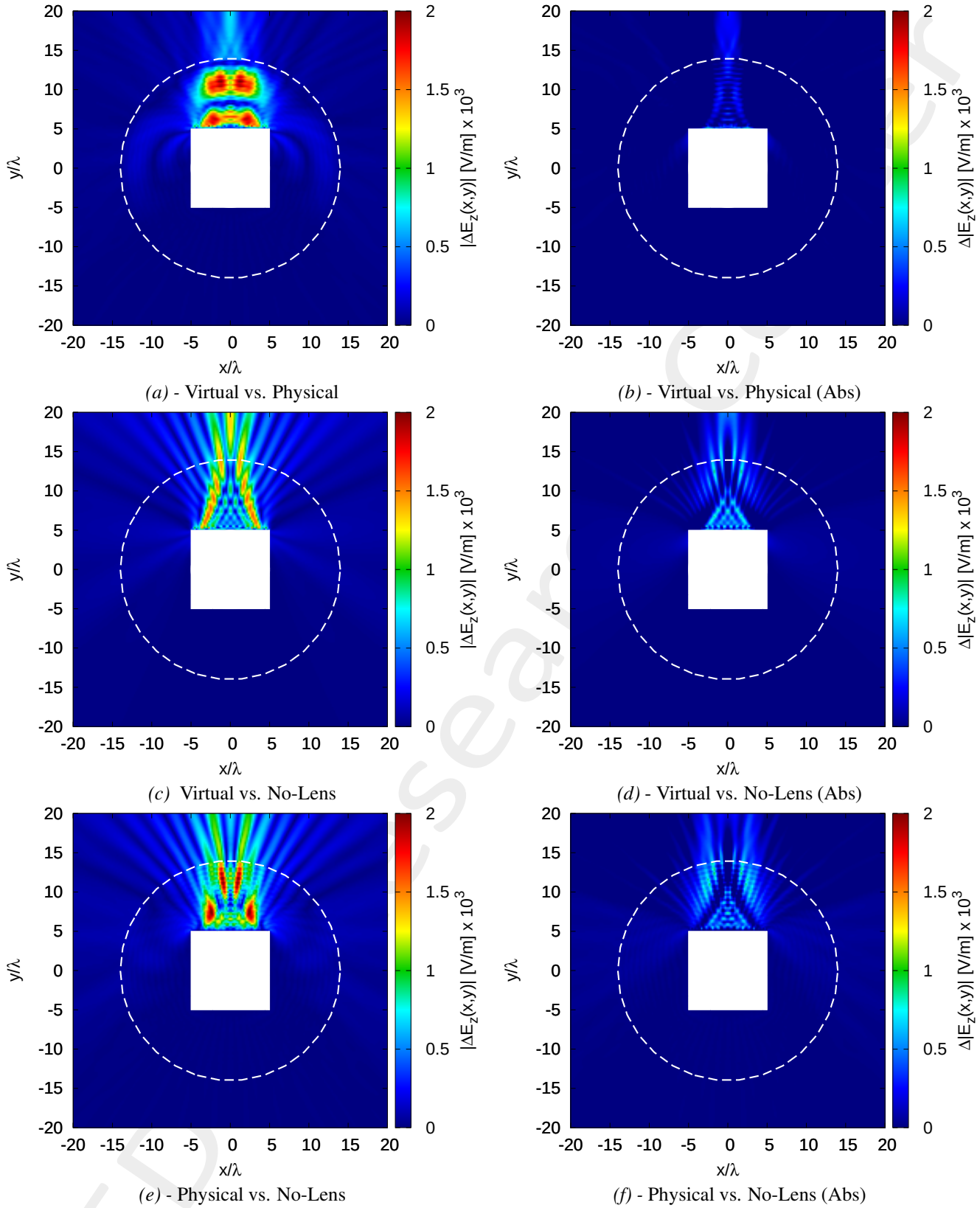

(a) - Virtual vs. Physical

(b) - Virtual vs. Physical (Abs)

(c) Virtual vs. No-Lens

(d) - Virtual vs. No-Lens (Abs)

(e) - Physical vs. No-Lens

(f) - Physical vs. No-Lens (Abs)

Figure 4: Near-Field difference pattern in the *(a)(b)* virtual vs. physical, *(c)(d)* virtual vs. no-lens and *(e)(f)* physical vs. no-lens. The difference pattern is computed for the *(a)(c)(e)* cases as $|\Delta E_z| \triangleq \left|E_z^{ref}(x,y) - E_z^{est}(x,y)\right|_{(x,y)\notin\Omega}$ while for the *(b)(d)(f)* cases as $\Delta|E_z| \triangleq \left[\left|E_z^{ref}(x,y)\right| - |E_z^{est}(x,y)|\right]_{(x,y)\notin\Omega}$

	Virtual	Physical	Physical (No Lens)
Directivity [dB]	13.41	13.32	5.28
SLL [dB]	−11.87	−10.47	−0.01
HPBW [deg]	7.07	6.86	23.89
FNBW [deg]	15.76	14.50	7.83
Field Matching Error ξ (7)	–	0.01	0.73
Field Matching Error χ (8)	–	0.33	1.29

Table I: Pattern values for the virtual, physical and physical (no lens) cases

2.1.2 Results - Geometry 2 - Internal Horizontal Rectangle

Parameters

- Number of elements: $N = 20$
- Physical Region
  - External radius: $L_{ext} = 14$ $[\lambda]$
  - External Lens boundary : $\partial\Omega_{ext} = \left\{(x, y) \in \mathbb{R} \mid \sqrt{x^2 + y^2} = L_{ext}\right\}$ $[\lambda]$
  - Internal Lens boundary: $\partial\Omega_{int} = \{(5; 2.5),\ (-5; 2.5);\ (-5; -2.5),\ (5, -2.5)\}$ $[\lambda]$
  - Number of points defining the external boundary: $n_{ext} = 30$
  - Number of points defining the internal boundary: $n_{int} = 4$

Results

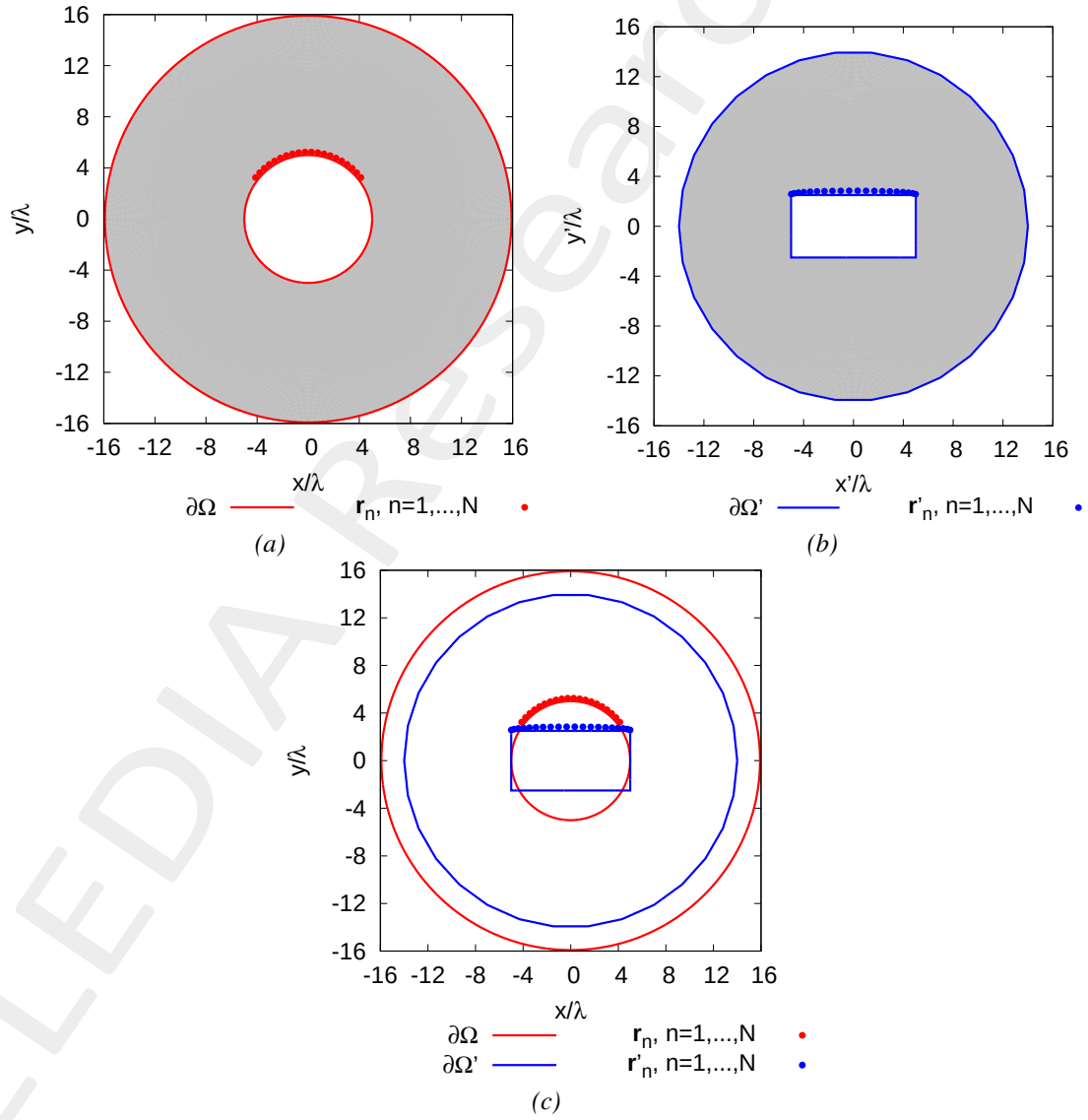

Figure 5: *(a)* Virtual, *(b)* Physical geometries and *(c)* the comparison

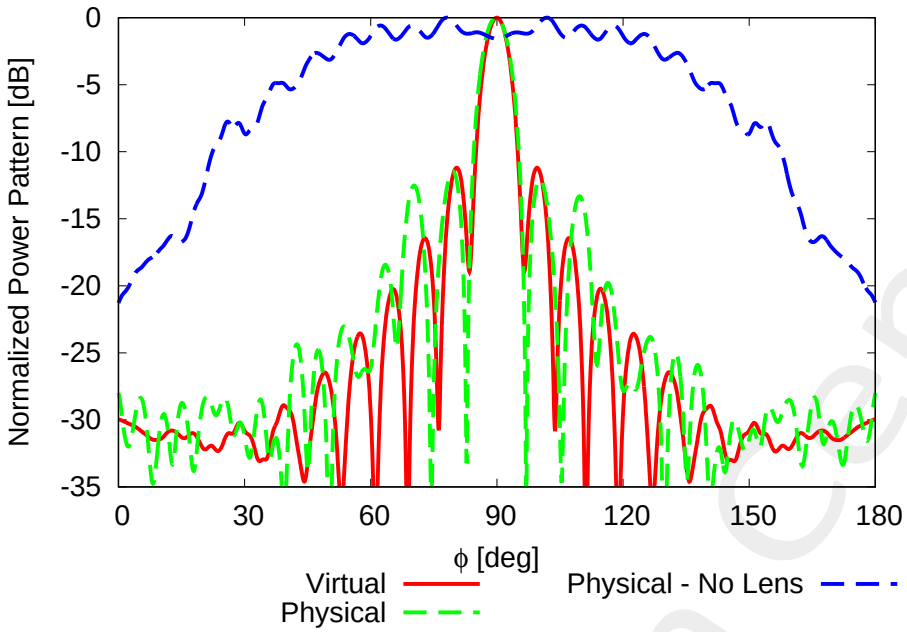

Figure 6: Far-Field Pattern for $\theta = 90$ [deg] and $\varphi \in [0, 180]$ [deg]

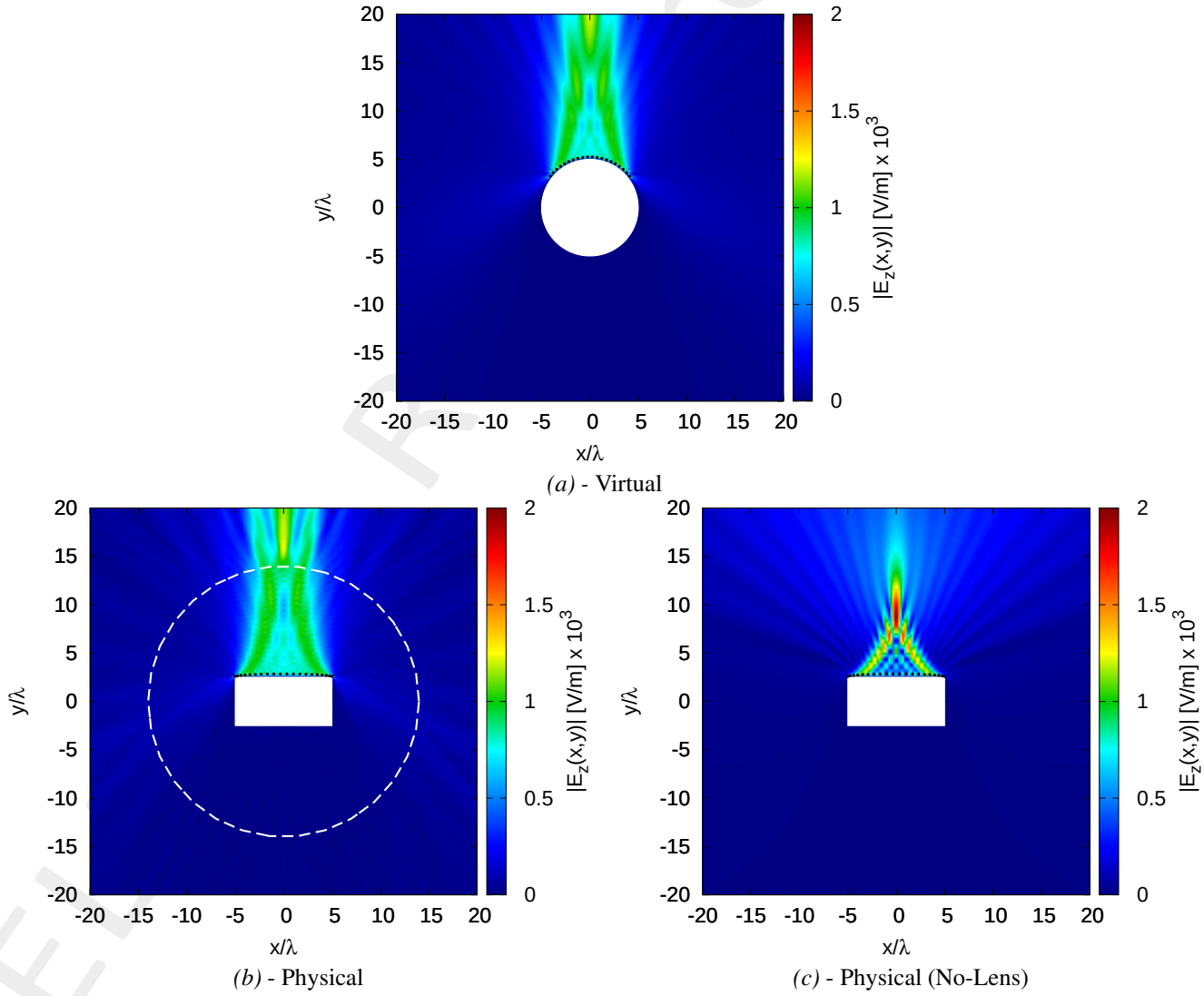

Figure 7: Near-Field pattern in the *(a)* virtual, *(b)* physical and *(c)* no-lens

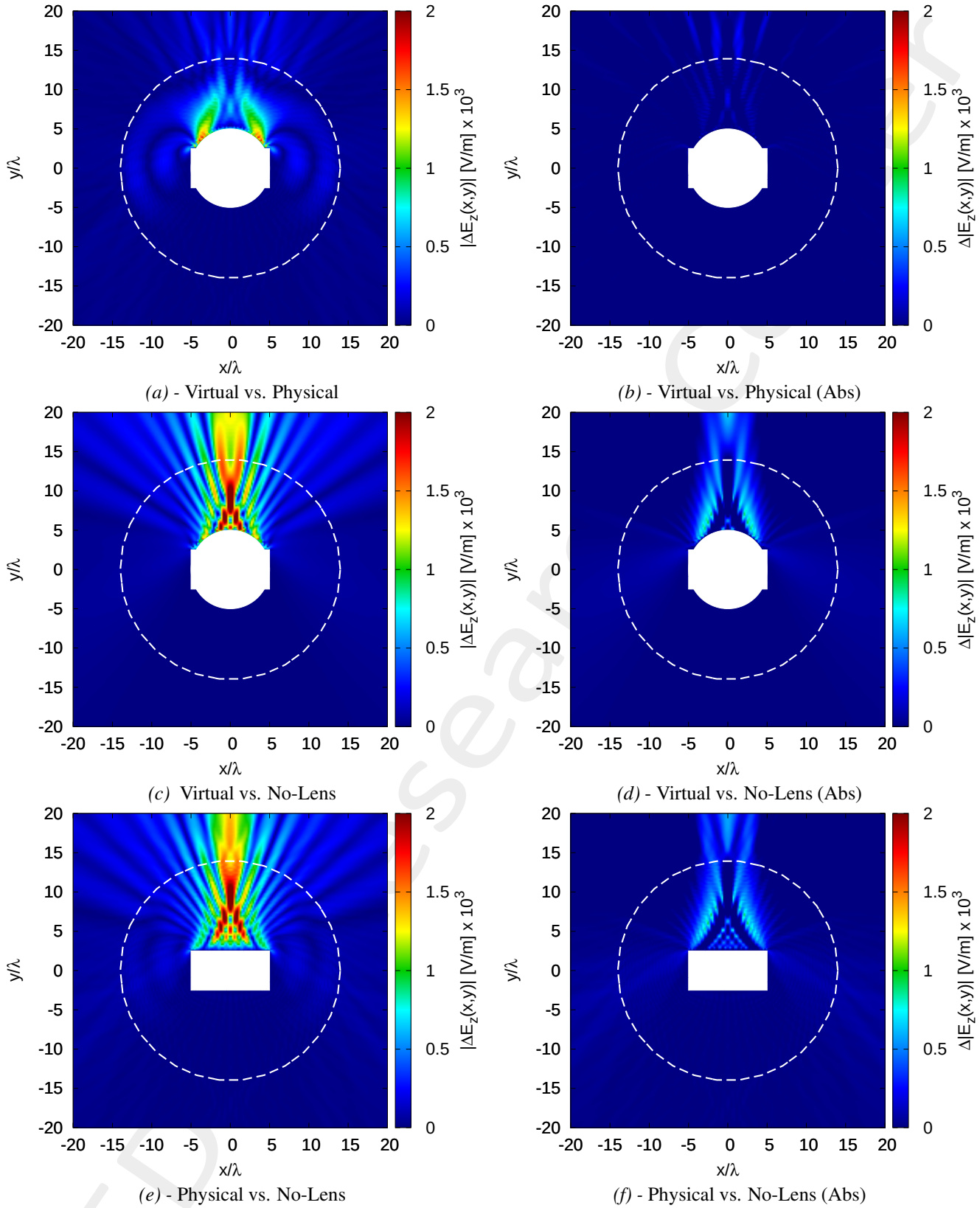

(a) - Virtual vs. Physical

(b) - Virtual vs. Physical (Abs)

(c) Virtual vs. No-Lens

(d) - Virtual vs. No-Lens (Abs)

(e) - Physical vs. No-Lens

(f) - Physical vs. No-Lens (Abs)

Figure 8: Near-Field difference pattern in the *(a)(b)* virtual vs. physical, *(c)(d)* virtual vs. no-lens and *(e)(f)* physical vs. no-lens. The difference pattern is computed for the *(a)(c)(e)* cases as $|\Delta E_z| \triangleq \left|E_z^{ref}(x,y) - E_z^{est}(x,y)\right|_{(x,y)\notin\Omega}$ while for the *(b)(d)(f)* cases as $\Delta|E_z| \triangleq \left[\left|E_z^{ref}(x,y)\right| - |E_z^{est}(x,y)|\right]_{(x,y)\notin\Omega}$

	Virtual	Physical	Physical (No Lens)
Directivity [dB]	14.09	13.59	3.64
SLL [dB]	−11.19	−11.45	−0.00
HPBW [deg]	5.91	6.61	78.22
FNBW [deg]	13.06	14.23	9.54
Field Matching Error ξ (7)	–	0.04	0.73
Field Matching Error χ (8)	–	0.13	1.98

Table II: Pattern values for the virtual, physical and physical (no lens) cases

2.1.3 Results - Geometry 3 - Internal Vertical Rectangle

Parameters

- Number of elements: $N = 20$
- Physical Region
  - External radius: $L_{ext} = 20$ $[\lambda]$
  - External Lens boundary : $\partial\Omega_{ext} = \left\{(x, y) \in \mathbb{R} \mid \sqrt{x^2 + y^2} = L_{ext}\right\}$ $[\lambda]$
  - Internal Lens boundary: $\partial\Omega_{int} = \{(2; 5),\ (-2; 5);\ (-2; -5),\ (2, -5)\}$ $[\lambda]$
  - Number of points defining the external boundary: $n_{ext} = 30$
  - Number of points defining the internal boundary: $n_{int} = 4$

Results

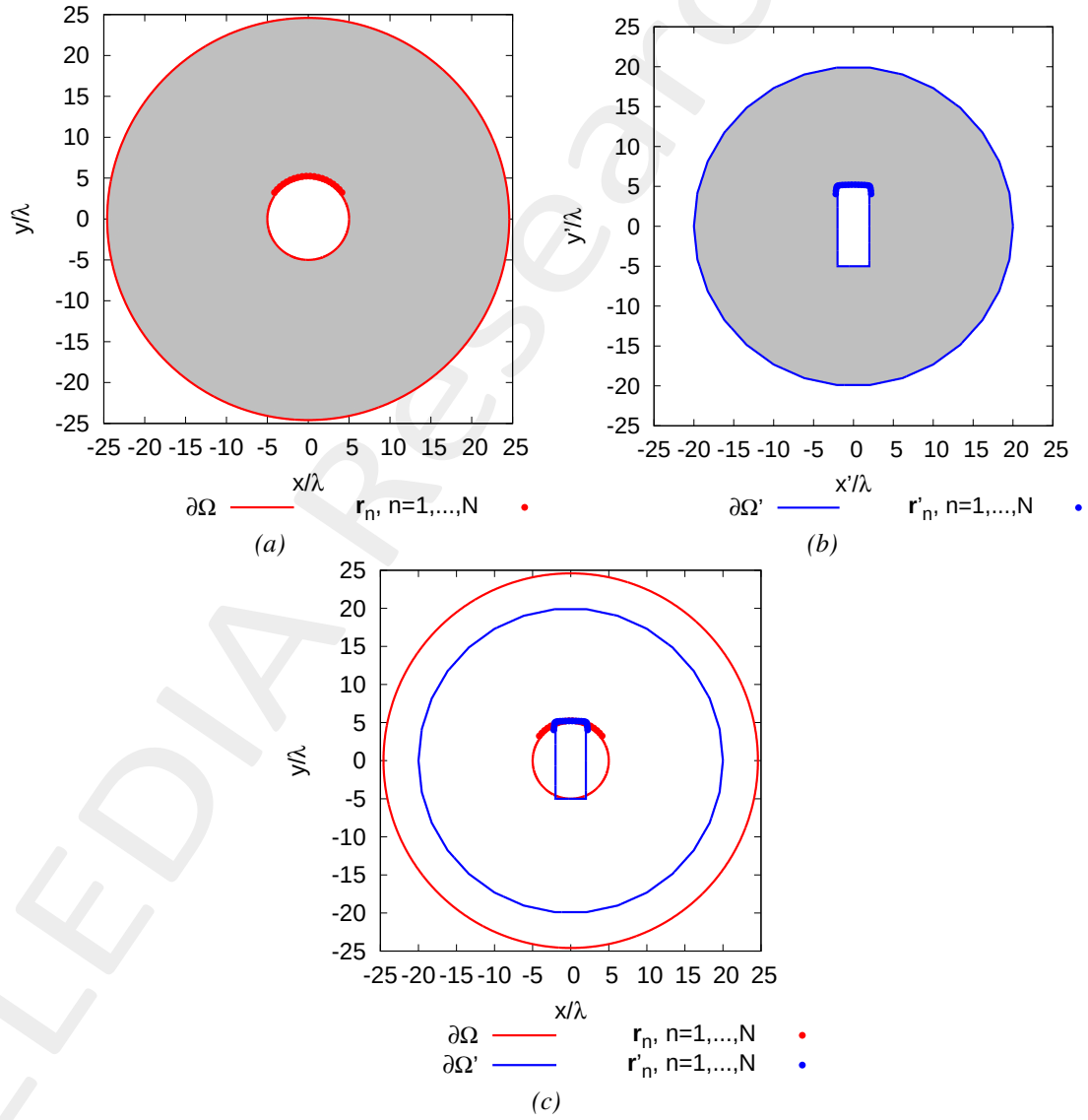

Figure 9: *(a)* Virtual, *(b)* Physical geometries and *(c)* the comparison

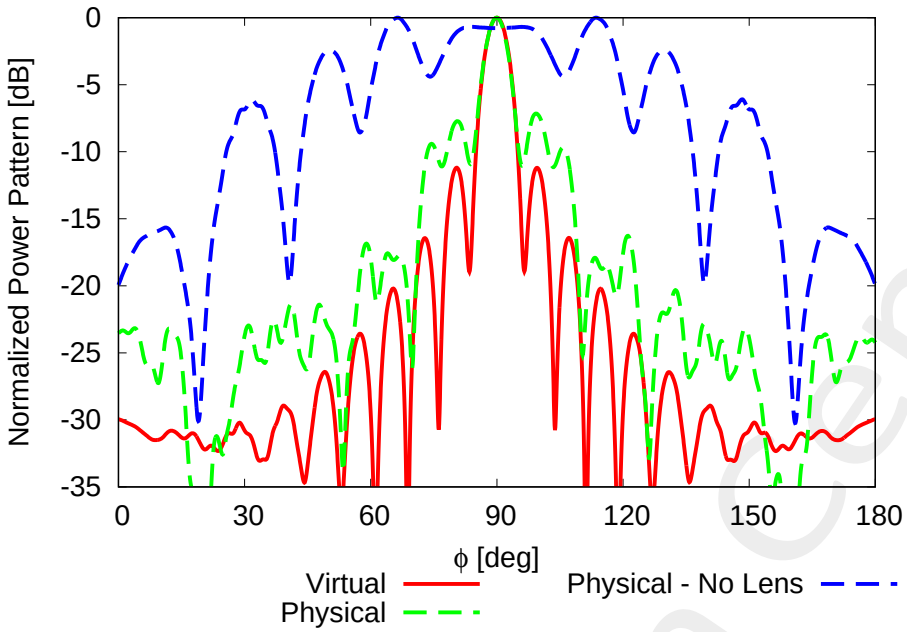

Figure 10: Far-Field Pattern for $\theta = 90$ [deg] and $\varphi \in [0, 180]$ [deg]

	Virtual	Physical	Physical (No Lens)
Directivity [dB]	14.09	12.71	4.81
SLL [dB]	-11.19	-7.15	-0.00
HPBW [deg]	5.91	5.82	10.02
FNBW [deg]	13.06	12.25	16.66
Field Matching Error ξ (7)	–	0.10	0.64
Field Matching Error χ (8)	–	3.38	3.49

Table III: Pattern values for the virtual, physical and physical (no lens) cases

2.1.4 Results - Geometry 4 - Internal Hexagon 1

Parameters

- Number of elements: $N = 20$
- Physical Region
  - External radius: $L_{ext} = 14$ $[\lambda]$
  - External Lens boundary : $\partial\Omega_{ext} = \left\{(x, y) \in \mathbb{R} \mid \sqrt{x^2 + y^2} = L_{ext}\right\}$ $[\lambda]$
  - Internal Lens boundary: $\partial\Omega_{int} = \{(5; 0),\ (2.5; 4.33);\ (-2.5; 4.33),\ (-5, 0),\ (-2.5; -4.33),\ (2.5; -4, 33)\}$ $[\lambda]$
  - Number of points defining the external boundary: $n_{ext} = 30$
  - Number of points defining the internal boundary: $n_{int} = 6$

Results

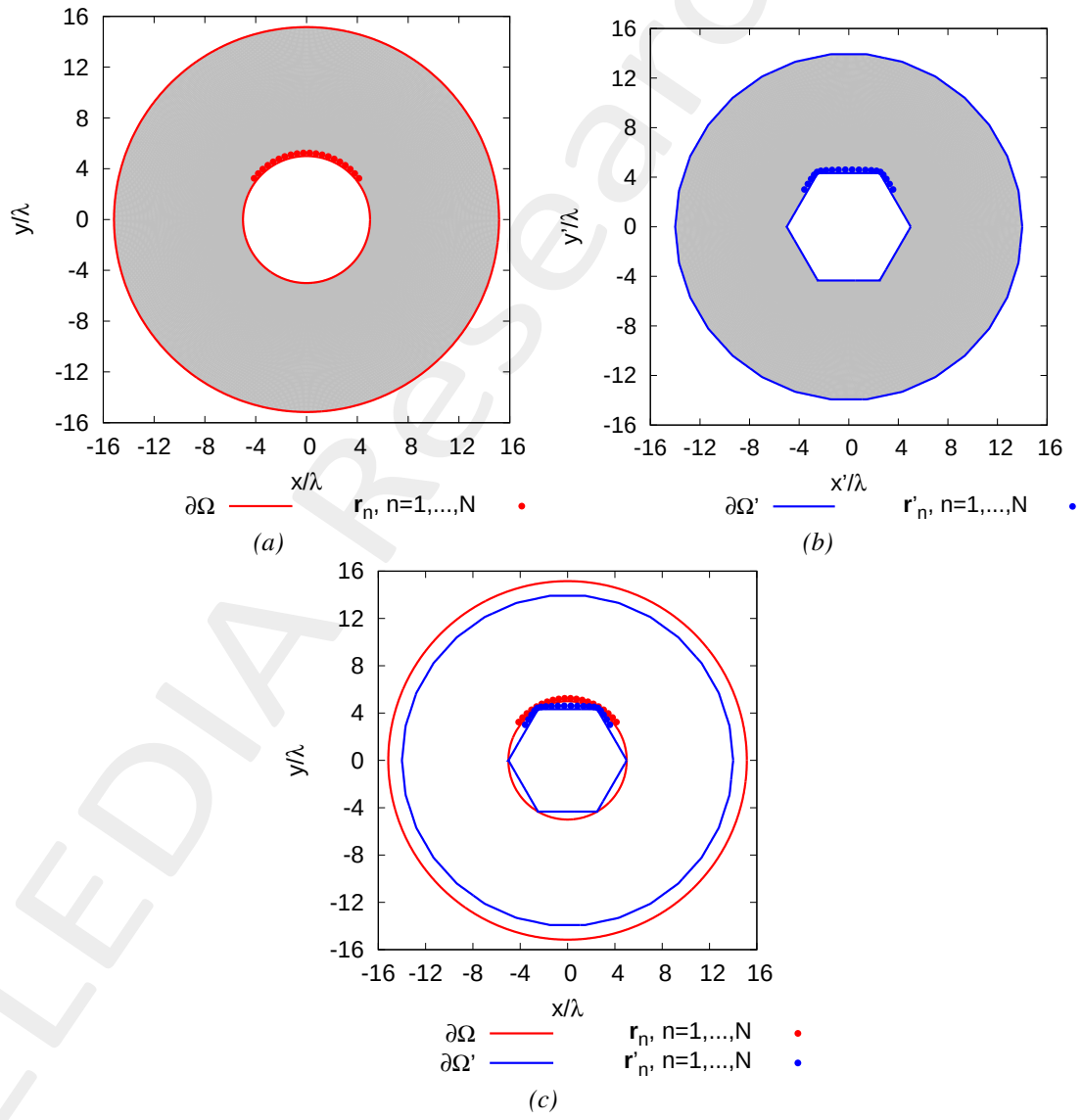

Figure 11: *(a)* Virtual, *(b)* Physical geometries and *(c)* the comparison

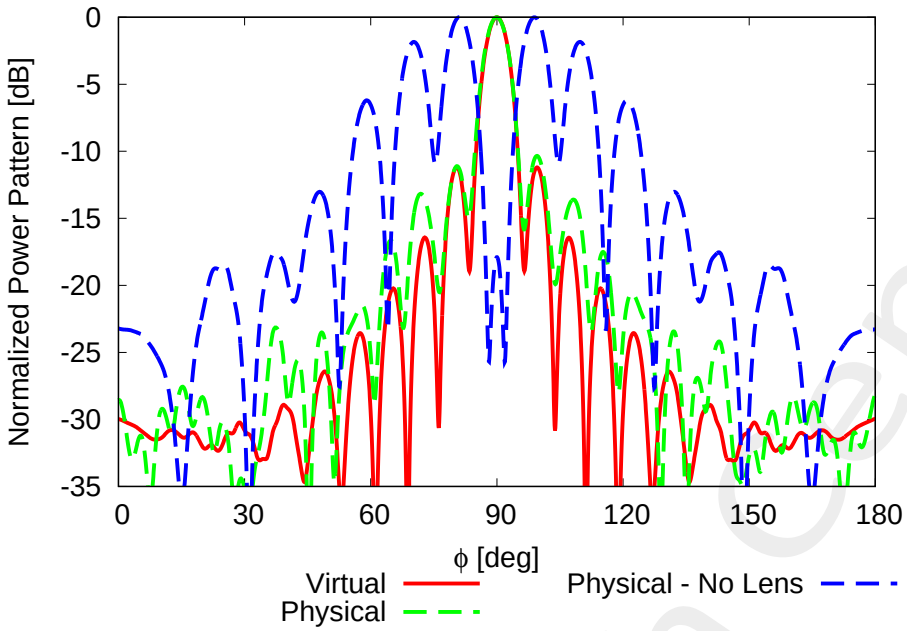

Figure 12: Far-Field Pattern for $\theta = 90$ [deg] and $\varphi \in [0, 180]$ [deg]

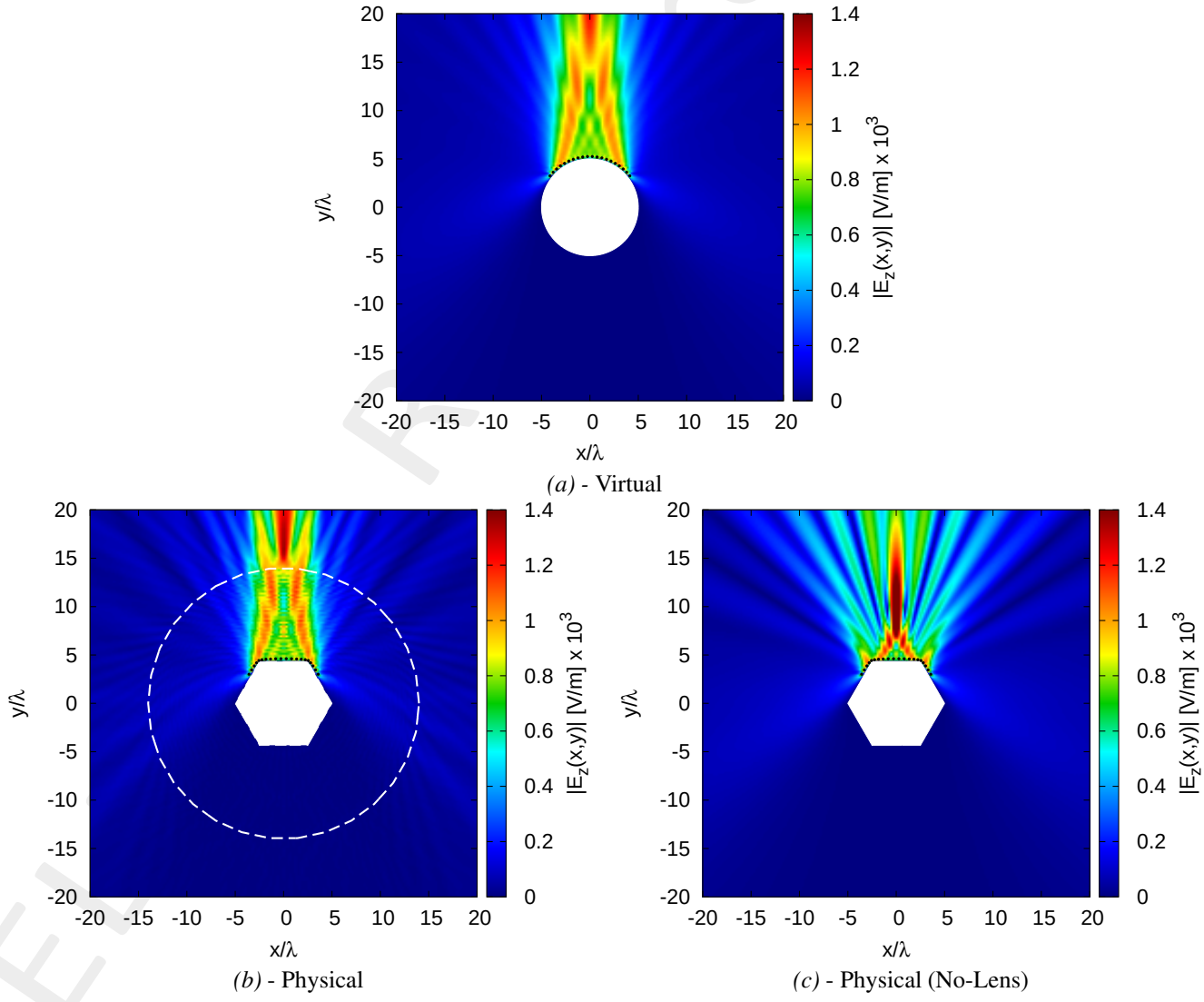

Figure 13: Near-Field pattern in the *(a)* virtual, *(b)* physical and *(c)* no-lens

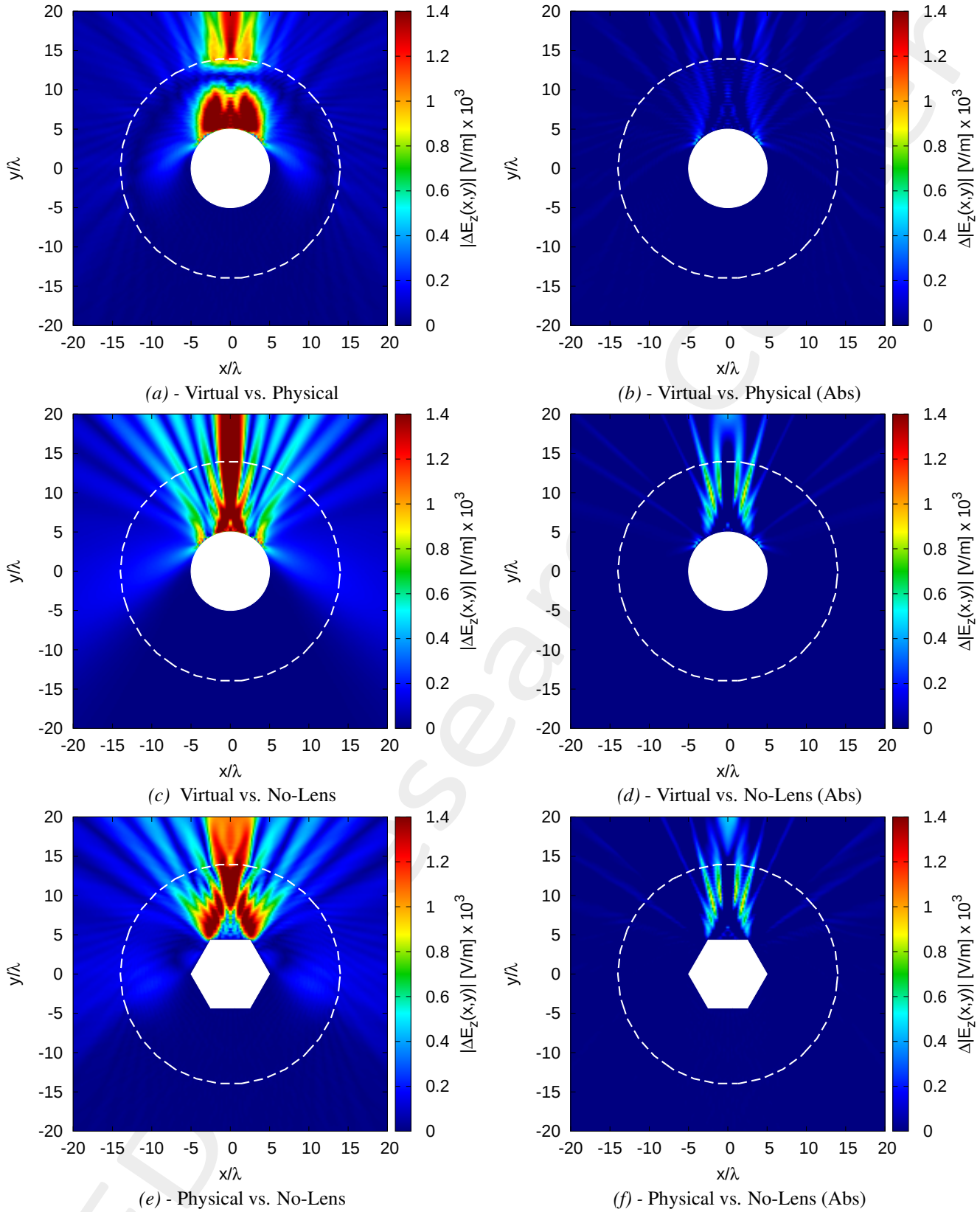

(a) - Virtual vs. Physical

(b) - Virtual vs. Physical (Abs)

(c) Virtual vs. No-Lens

(d) - Virtual vs. No-Lens (Abs)

(e) - Physical vs. No-Lens

(f) - Physical vs. No-Lens (Abs)

Figure 14: Near-Field difference pattern in the *(a)(b)* virtual vs. physical, *(c)(d)* virtual vs. no-lens and *(e)(f)* physical vs. no-lens. The difference pattern is computed for the *(a)(c)(e)* cases as $|\Delta E_z| \triangleq \left|E_z^{ref}(x,y) - E_z^{est}(x,y)\right|_{(x,y)\notin\Omega}$ while for the *(b)(d)(f)* cases as $\Delta|E_z| \triangleq \left[\left|E_z^{ref}(x,y)\right| - |E_z^{est}(x,y)|\right]_{(x,y)\notin\Omega}$

	Virtual	Physical	Physical (No Lens)
Directivity [dB]	14.09	13.64	8.77
SLL [dB]	−11.20	−10.34	−0.01
HPBW [deg]	5.91	6.04	6.02
FNBW [deg]	13.06	13.24	12.79
Field Matching Error ξ (7)	–	0.02	1.08
Field Matching Error χ (8)	–	1.21	2.07

Table IV: Pattern values for the virtual, physical and physical (no lens) cases

2.1.5 Results - Geometry 5 - Internal Hexagon 2

Parameters

- Number of elements: $N = 20$
- Physical Region
  - External radius: $L_{ext} = 14$ $[\lambda]$
  - External Lens boundary : $\partial\Omega_{ext} = \left\{(x, y) \in \mathbb{R} \mid \sqrt{x^2 + y^2} = L_{ext}\right\}$ $[\lambda]$
  - Internal Lens boundary: $\partial\Omega_{int} = \{(4.33; 2.5),\ (0; 5);\ (-4.33; 2.5),\ (-4.33, -2.5),\ (0; -5),\ (4.33; -2.55)\}$ $[\lambda]$
  - Number of points defining the external boundary: $n_{ext} = 30$
  - Number of points defining the internal boundary: $n_{int} = 6$

Results

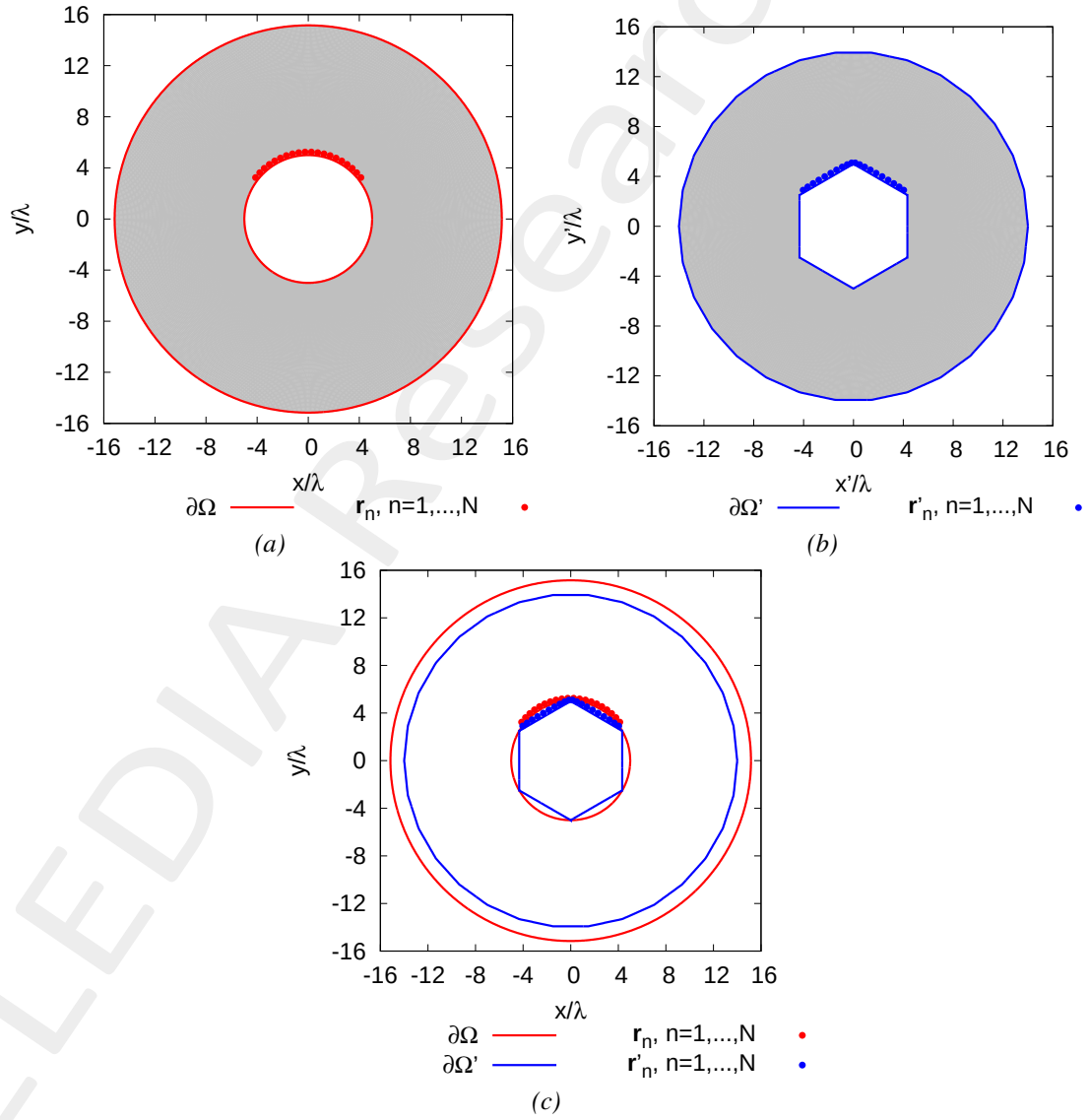

Figure 15: *(a)* Virtual, *(b)* Physical geometries and *(c)* the comparison

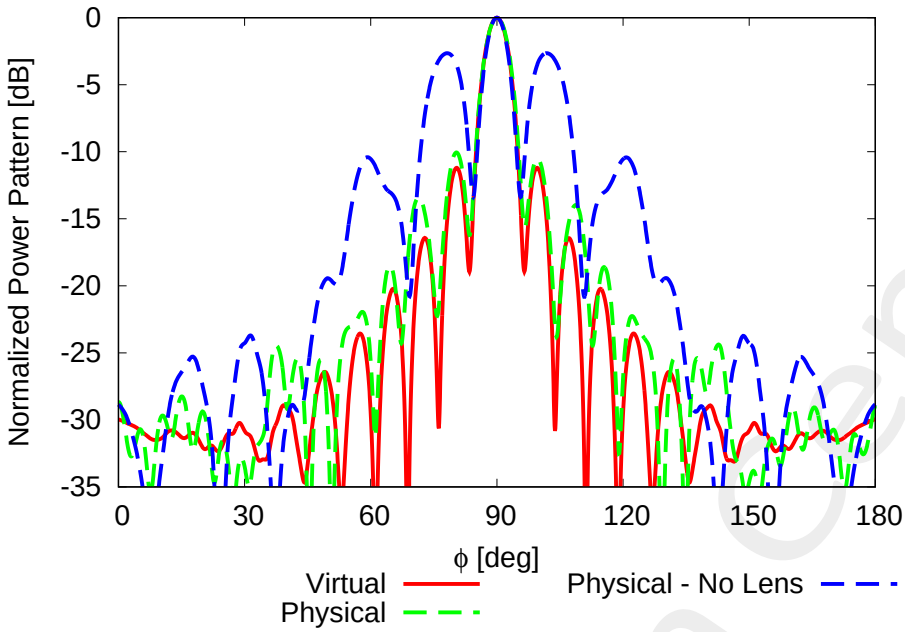

Figure 16: Far-Field Pattern for $\theta = 90$ [deg] and $\varphi \in [0, 180]$ [deg]

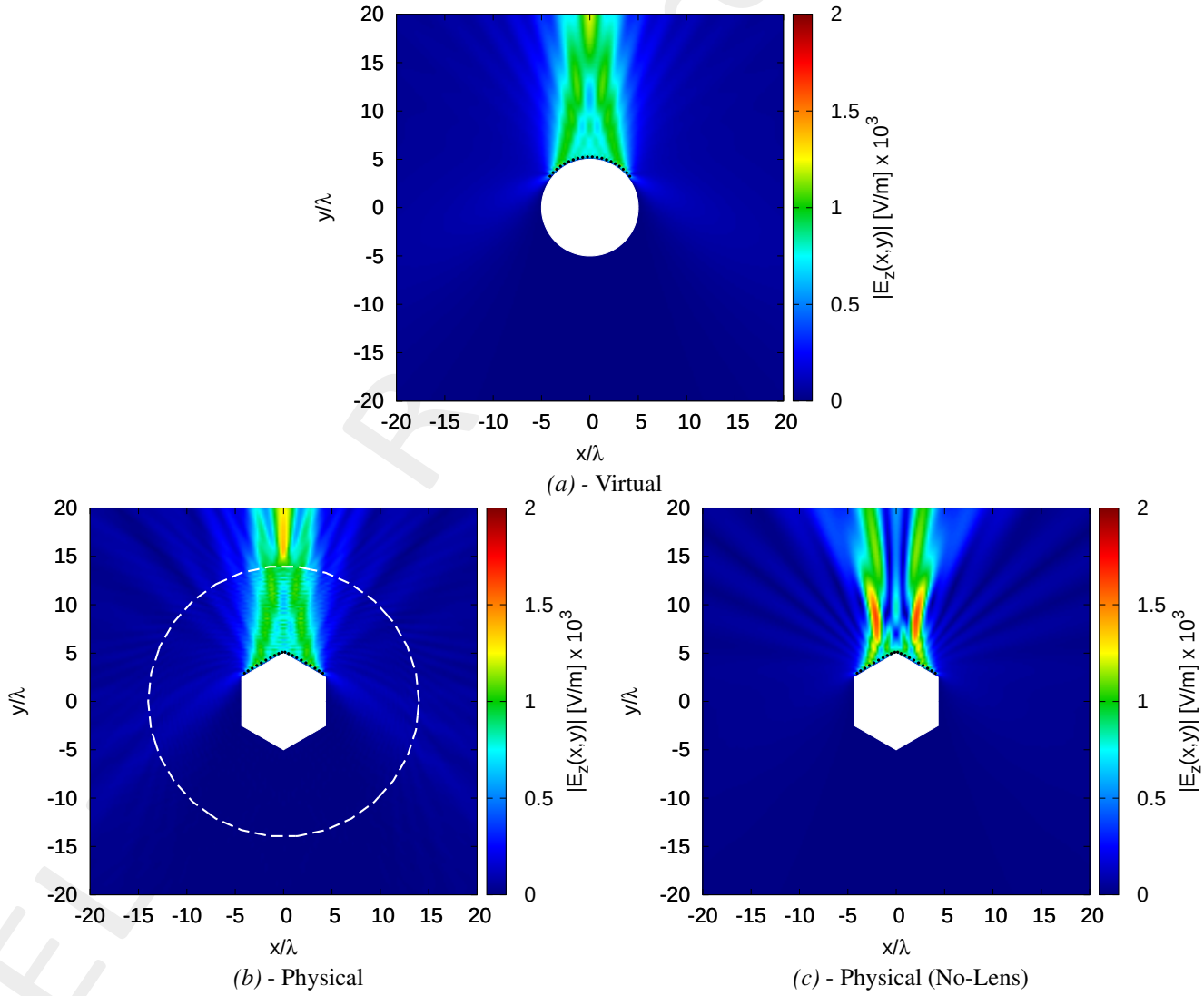

Figure 17: Near-Field pattern in the *(a)* virtual, *(b)* physical and *(c)* no-lens

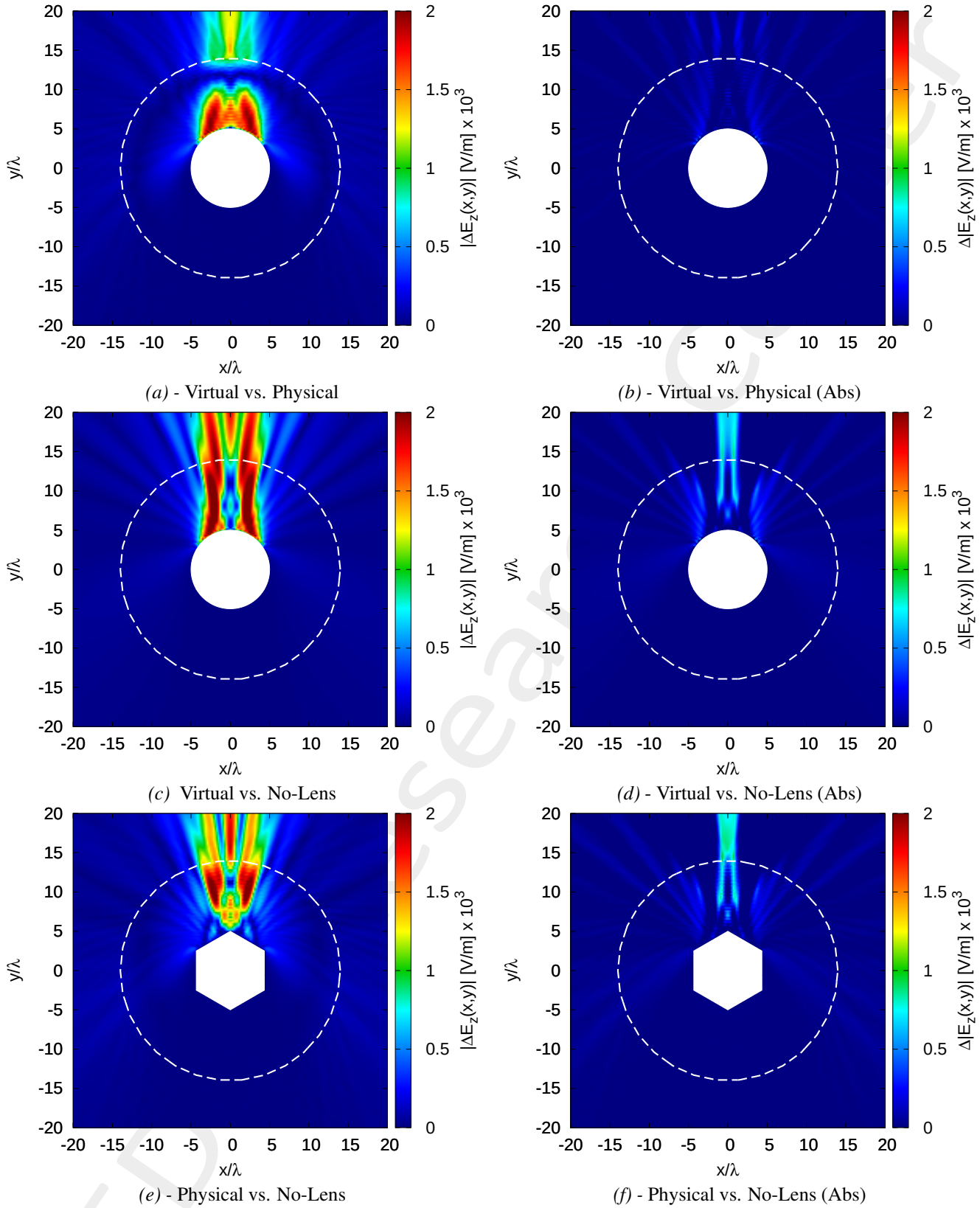

(a) - Virtual vs. Physical

(b) - Virtual vs. Physical (Abs)

(c) Virtual vs. No-Lens

(d) - Virtual vs. No-Lens (Abs)

(e) - Physical vs. No-Lens

(f) - Physical vs. No-Lens (Abs)

Figure 18: Near-Field difference pattern in the *(a)(b)* virtual vs. physical, *(c)(d)* virtual vs. no-lens and *(e)(f)* physical vs. no-lens. The difference pattern is computed for the *(a)(c)(e)* cases as $|\Delta E_z| \triangleq \left|E_z^{ref}(x,y) - E_z^{est}(x,y)\right|_{(x,y)\notin\Omega}$ while for the *(b)(d)(f)* cases as $\Delta|E_z| \triangleq \left[\left|E_z^{ref}(x,y)\right| - |E_z^{est}(x,y)|\right]_{(x,y)\notin\Omega}$

	Virtual	Physical	Physical (No Lens)
Directivity [dB]	14.09	13.68	10.36
SLL [dB]	-11.20	-10.06	-2.65
HPBW [deg]	5.91	6.07	5.55
FNBW [deg]	13.06	13.15	11.26
Field Matching Error ξ (7)	$-$	0.02	0.37
Field Matching Error χ (8)	$-$	1.16	3.10

Table V: Pattern values for the virtual, physical and physical (no lens) cases

2.1.6 Results - Geometry 6 - Internal Octagon

Parameters

- Number of elements: $N = 20$
- Physical Region
  - External radius: $L_{ext} = 14$ $[\lambda]$
  - External Lens boundary : $\partial\Omega_{ext} = \left\{(x, y) \in \mathbb{R} \mid \sqrt{x^2 + y^2} = L_{ext}\right\}$ $[\lambda]$
  - Internal Lens boundary:

$$\partial\Omega_{int} = \{(4.61; 1.91),\ (1.91; 4.61);\ (-1.91; 4.61),\ (-4.61, 1.91),\ (-4.61; -1.91),\ (-1.91; -4.61),\ (1.91; -4.61),\ (4.61; -1.91)\}\ [\lambda]$$

  - Number of points defining the external boundary: $n_{ext} = 30$
  - Number of points defining the internal boundary: $n_{int} = 8$

Results

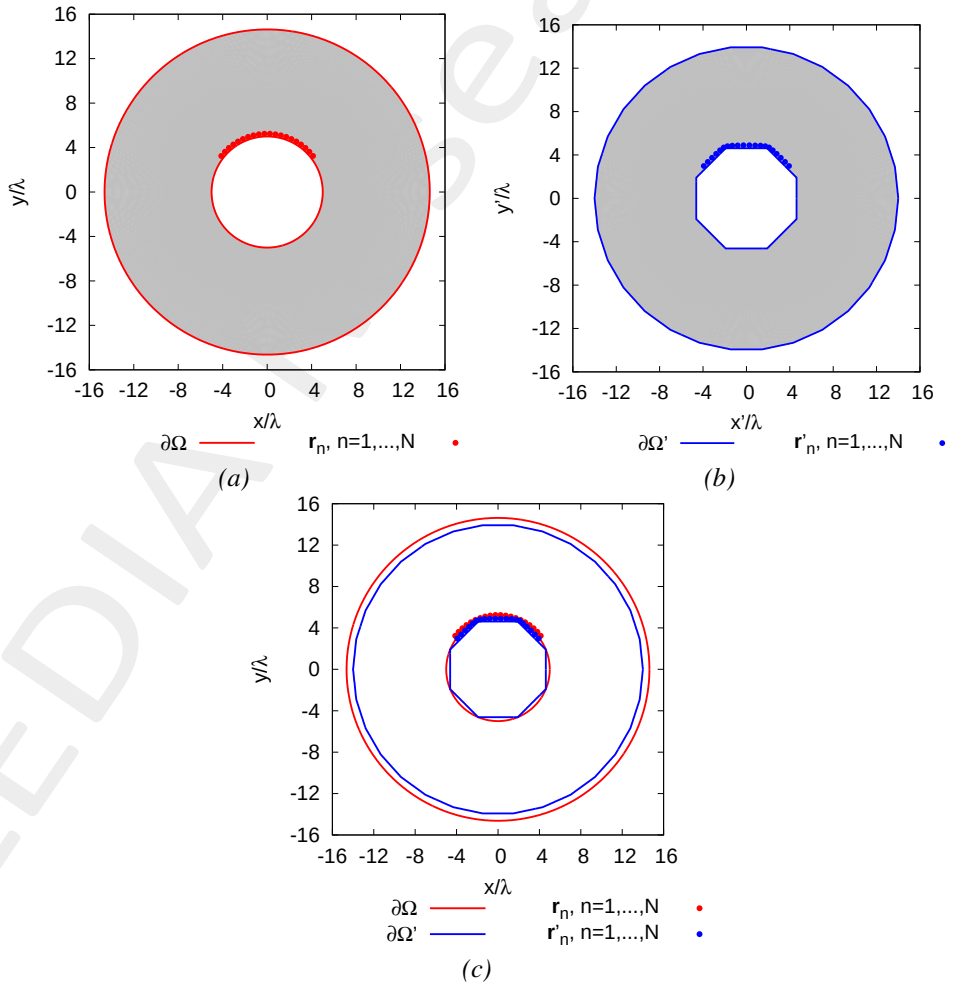

Figure 19: *(a)* Virtual, *(b)* Physical geometries and *(c)* the comparison

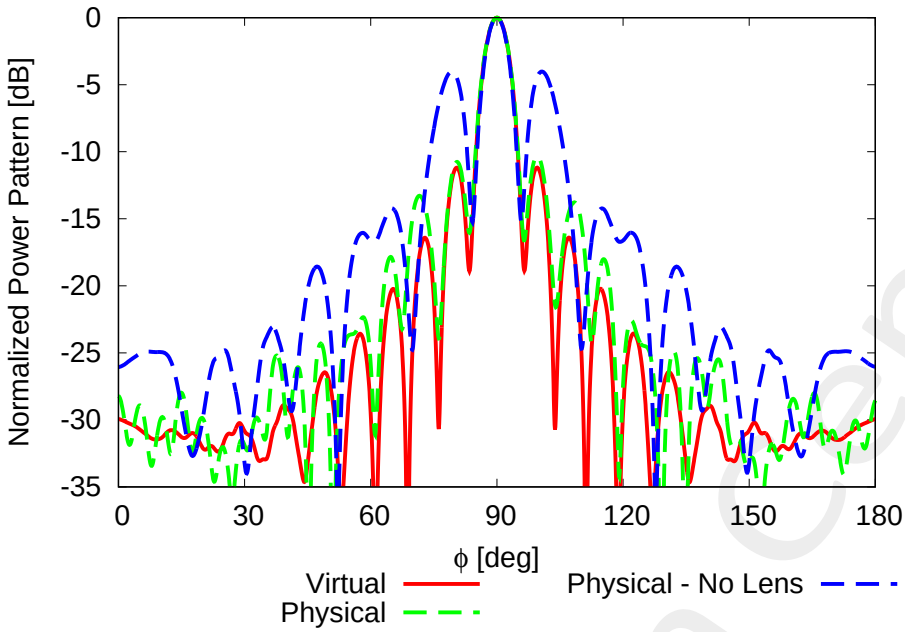

Figure 20: Far-Field Pattern for $\theta = 90$ [deg] and $\varphi \in [0, 180]$ [deg]

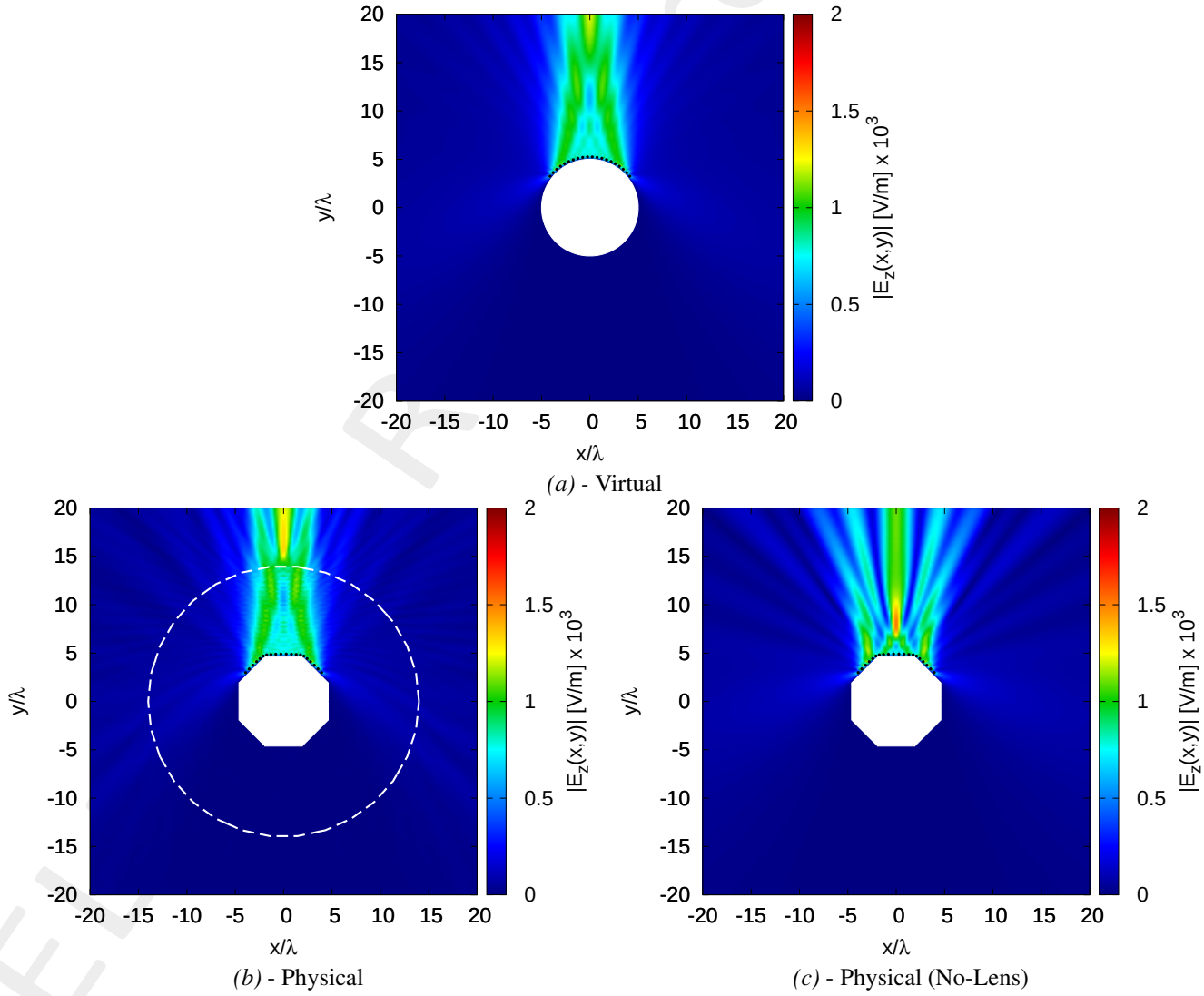

Figure 21: Near-Field pattern in the *(a)* virtual, *(b)* physical and *(c)* no-lens

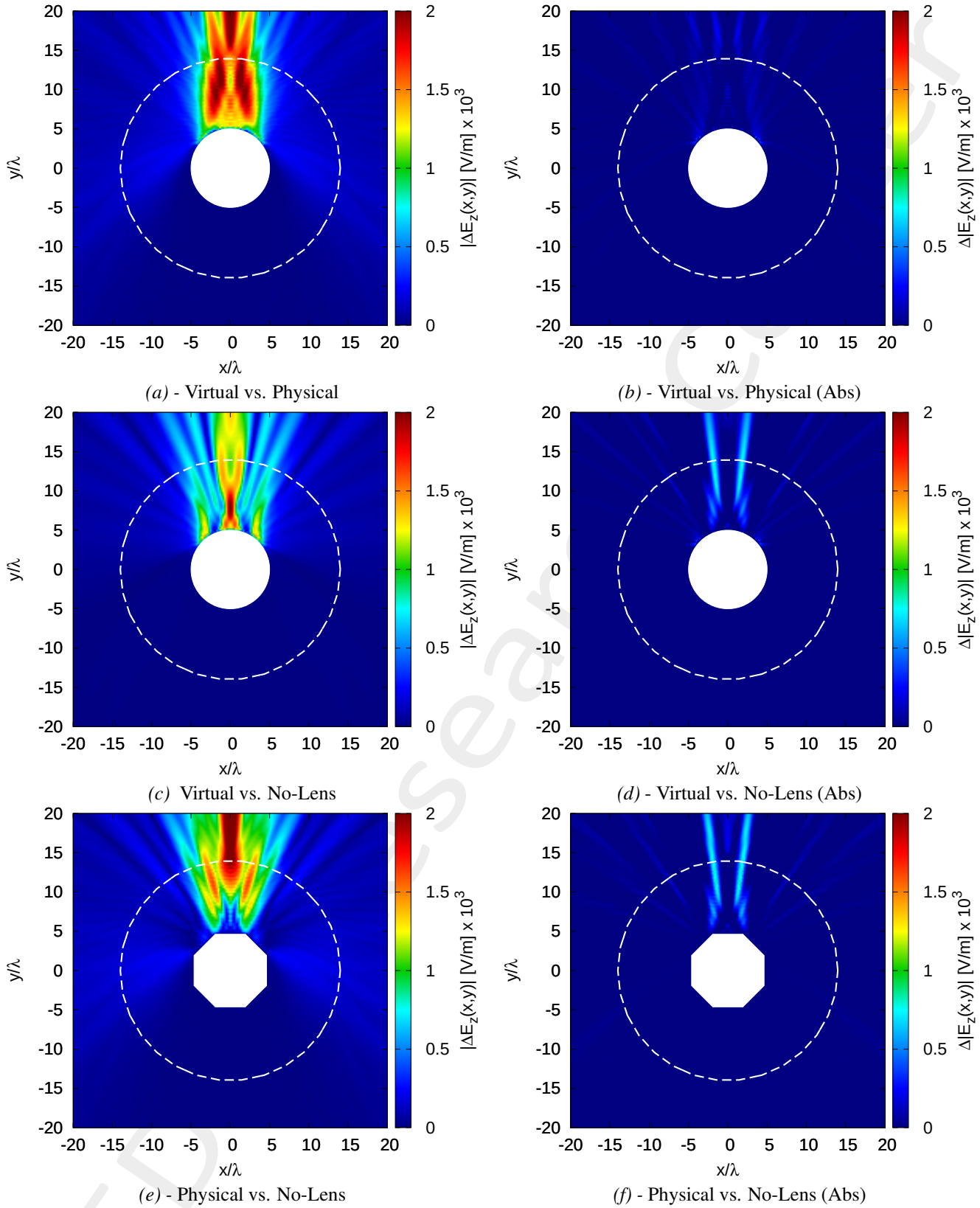

(a) - Virtual vs. Physical

(b) - Virtual vs. Physical (Abs)

(c) Virtual vs. No-Lens

(d) - Virtual vs. No-Lens (Abs)

(e) - Physical vs. No-Lens

(f) - Physical vs. No-Lens (Abs)

Figure 22: Near-Field difference pattern in the *(a)(b)* virtual vs. physical, *(c)(d)* virtual vs. no-lens and *(e)(f)* physical vs. no-lens. The difference pattern is computed for the *(a)(c)(e)* cases as $|\Delta E_z| \triangleq \left|E_z^{ref}(x,y) - E_z^{est}(x,y)\right|_{(x,y)\notin\Omega}$ while for the *(b)(d)(f)* cases as $\Delta|E_z| \triangleq \left[\left|E_z^{ref}(x,y)\right| - |E_z^{est}(x,y)|\right]_{(x,y)\notin\Omega}$

	Virtual	Physical	Physical (No Lens)
Directivity [dB]	14.09	13.73	11.73
SLL [dB]	-11.19	-10.32	-4.02
HPBW [deg]	5.91	6.00	5.67
FNBW [deg]	13.06	13.06	11.62
Field Matching Error ξ (7)	$-$	0.02	0.22
Field Matching Error χ (8)	$-$	3.01	1.67

Table VI: Pattern values for the virtual, physical and physical (no lens) cases

2.1.7 Results - Geometry 7 - Internal Triangle Down

Parameters

- Number of elements: $N = 20$
- Physical Region
  - External radius: $L_{ext} = 14$ $[\lambda]$
  - External Lens boundary : $\partial\Omega_{ext} = \left\{(x, y) \in \mathbb{R} \mid \sqrt{x^2 + y^2} = L_{ext}\right\}$ $[\lambda]$
  - Internal Lens boundary: $\partial\Omega_{int} = \{(4.33; 2.5),\ (-4.33; 2.5);\ (-2.16; -1.25),\ (0, -5),\ (2.16; -1.25)\}$ $[\lambda]$
  - Number of points defining the external boundary: $n_{ext} = 30$
  - Number of points defining the internal boundary: $n_{int} = 5$

Results

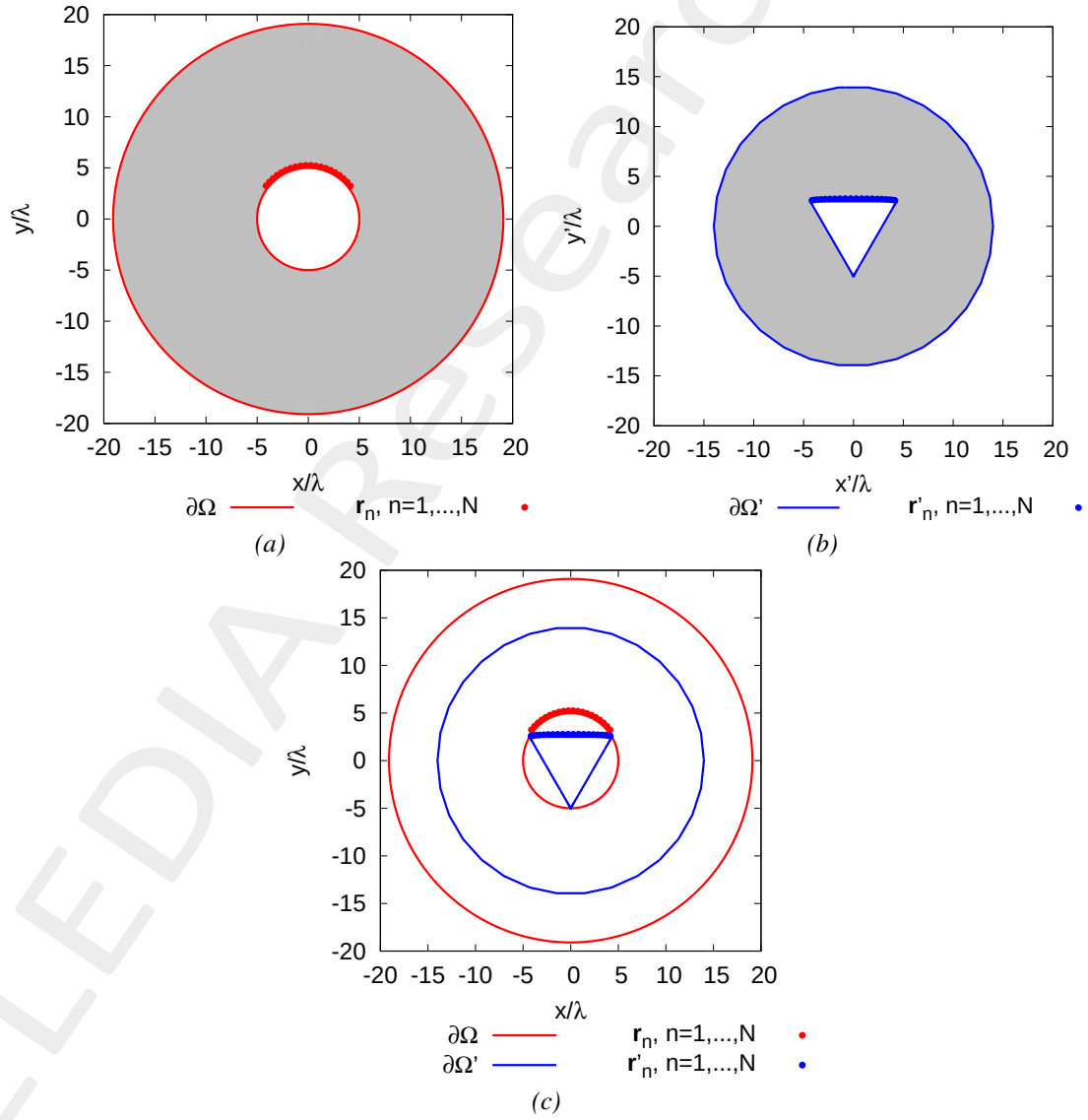

Figure 23: *(a)* Virtual, *(b)* Physical geometries and *(c)* the comparison

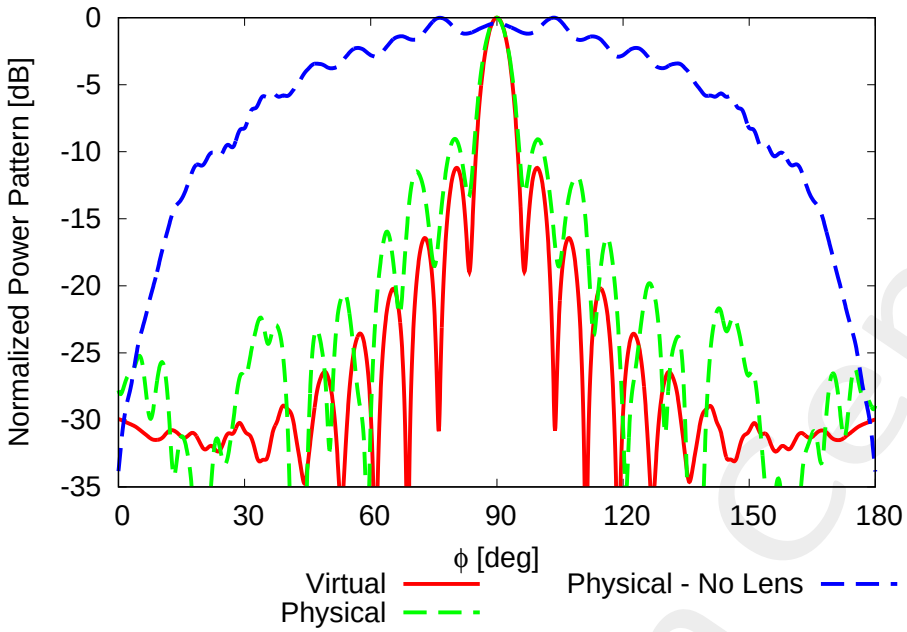

Figure 24: Far-Field Pattern for $\theta = 90$ [deg] and $\varphi \in [0, 180]$ [deg]

	Virtual	Physical	Physical (No Lens)
Directivity [dB]	14.09	13.11	3.95
SLL [dB]	-11.20	-9.04	-0.01
HPBW [deg]	5.91	6.31	72.30
FNBW [deg]	13.06	13.24	12.43
Field Matching Error ξ (7)	–	0.05	0.70
Field Matching Error χ (8)	–	0.43	2.18

Table VII: Pattern values for the virtual, physical and physical (no lens) cases

2.1.8 Results - Geometry 8 - Internal Triangle Up

Parameters

- Number of elements: $N = 20$
- Physical Region
  - External radius: $L_{ext} = 14$ $[\lambda]$
  - External Lens boundary : $\partial\Omega_{ext} = \left\{(x, y) \in \mathbb{R} \mid \sqrt{x^2 + y^2} = L_{ext}\right\}$ $[\lambda]$
  - Internal Lens boundary: $\partial\Omega_{int} = \{(2.16; 1.25), (0; 5); (-2.16; 1.25), (-4.33, -2.5), (4.33; -2.5)\}$ $[\lambda]$
  - Number of points defining the external boundary: $n_{ext} = 30$
  - Number of points defining the internal boundary: $n_{int} = 5$

Results

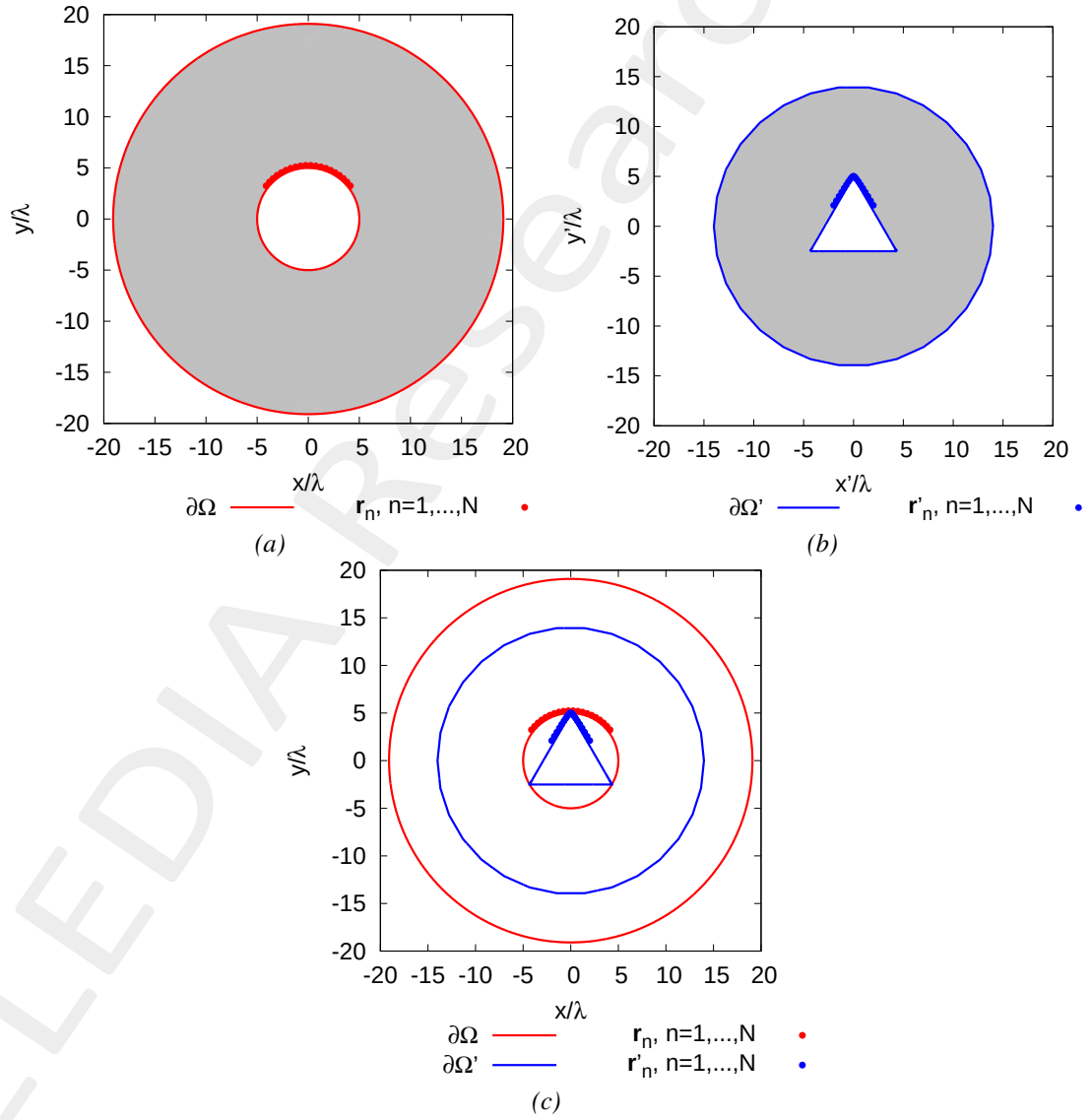

Figure 25: *(a)* Virtual, *(b)* Physical geometries and *(c)* the comparison

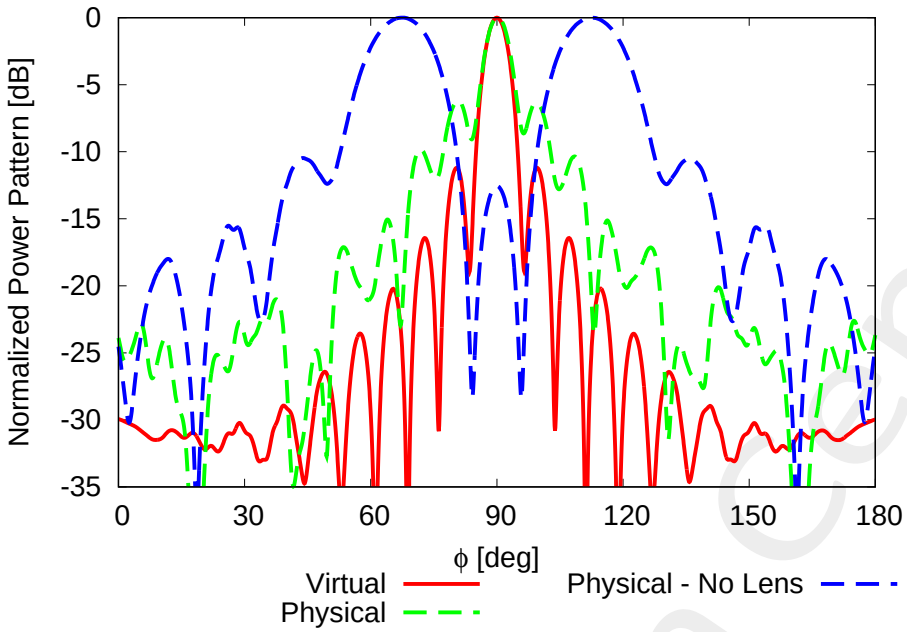

Figure 26: Far-Field Pattern for $\theta = 90$ [deg] and $\varphi \in [0, 180]$ [deg]

	Virtual	Physical	Physical (No Lens)
Directivity [dB]	14.09	12.02	6.88
SLL [dB]	-11.20	-6.19	-0.00
HPBW [deg]	5.91	6.40	16.74
FNBW [deg]	13.06	12.34	34.58
Field Matching Error ξ (7)	–	0.13	1.30
Field Matching Error χ (8)	–	0.29	2.05

Table VIII: Pattern values for the virtual, physical and physical (no lens) cases

3 Conclusions

An innovative transformation electromagnetics methodology based on the Schwarz-Christoffel theory has been proposed to design conformal phased arrays. The numerical results have shown the effectiveness and the potential of the proposed method.

References

[1] M. Salucci, F. Boulos, A. Polo, and G. Oliveri, “Conformal transformation electromagnetics based on Schwarz-Christoffel mapping for the synthesis of doubly-connected metalenses,” *IEEE Trans. Antennas Propag.*, vol. 68, no. 3, pp. 1836-1850, Mar. 2020.

[2] M. Salucci, L. Tenuti, G. Gottardi, A. Hannan, and A. Massa, "System-by-design method for efficient linear array miniaturisation through low-complexity isotropic lenses" *Electronic Letters*, vol. 55, no. 8, pp. 433-434, May 2019.

[3] M. Salucci, G. Oliveri, N. Anselmi, and A. Massa, "Material-by-design synthesis of conformal miniaturized linear phased arrays," *IEEE Access*, vol. 6, pp. 26367-26382, 2018.

[4] M. Salucci, G. Oliveri, N. Anselmi, G. Gottardi, and A. Massa, "Performance enhancement of linear active electronically-scanned arrays by means of MbD-synthesized metalenses," *Journal of Electromagnetic Waves and Applications*, vol. 32, no. 8, pp. 927-955, 2018.

[5] G. Oliveri, M. Salucci, N. Anselmi and A. Massa, "Multiscale System-by-Design synthesis of printed WAIMs for waveguide array enhancement," *IEEE J. Multiscale Multiphysics Computat. Techn.*, vol. 2, pp. 84-96, 2017.

[6] G. Oliveri, F. Viani, N. Anselmi, and A. Massa, "Synthesis of multi-layer WAIM coatings for planar phased arrays within the system-by-design framework," *IEEE Trans. Antennas Propag.*, vol. 63, no. 6, pp. 2482-2496, June 2015.

[7] A. Massa and G. Oliveri, "Metamaterial-by-Design: Theory, methods, and applications to communications and sensing - Editorial," *EPJ Applied Metamaterials*, vol. 3, no. E1, pp. 1-3, 2016.

[8] G. Oliveri, E. T. Bekele, M. Salucci, and A. Massa, "Transformation electromagnetics miniaturization of sectoral and conical horn antennas," *IEEE Trans. Antennas Propag.*, vol. 64, no. 4, pp. 1508-1513, April 2016.

[9] G. Oliveri, E. T. Bekele, M. Salucci, and A. Massa, "Array miniaturization through QCTO-SI metamaterial radomes" *IEEE Trans. Antennas Propag.*, vol. 63, no. 8, pp. 3465-3476, Aug. 2015.

[10] L. Tenuti, M. Salucci, G. Oliveri, P. Rocca, and A. Massa, “Surrogate- assisted optimization of metamaterial devices for advanced antenna Systems,” Proc. 2015 IEEE Symposium Series on Computational Intelligence (IEEE SSCI 2015), Cape Town, South Africa, pp. 1154-1156, Dec. 8-10, 2015.

[11] G. Oliveri, L. Tenuti, M. Salucci, and A. Massa, “Innovative antenna architectures exploiting metamaterials for new generation radars,” 10th European Conference on Antennas and Propagation (EUCAP 2016), Davos, Switzerland, pp. 1-3, April 11-15, 2016.

[12] M. Salucci, G. Oliveri, H. Ahmadi, and A. Massa, "Conformal transformation of linear arrays through QCTO-based design tools," Proc. 2016 IEEE AP-S International Symposium and USNC-URSI Radio Science Meeting, Fajardo, Puerto Rico, pp. 1083- 1084, July 26 - July 1, 2016.

[13] M. Salucci, L. Tenuti, E. Bekele, and G. Oliveri, "Enhancement of linear arrays through MbD metamaterial coatings," Proc. 2016 IEEE AP-S International Symposium and USNC-URSI Radio Science Meeting, Fajardo, Puerto Rico, pp. 1089- 1090, July 26 - July 1, 2016.

[14] P. Rocca, N. Anselmi, A. Polo, and A. Massa, "An irregular two-sizes square tiling method for the design of isophoric phased arrays," *IEEE Trans. Antennas Propag.*, vol. 68, no. 6, pp. 4437-4449, Jun. 2020.

[15] P. Rocca, N. Anselmi, A. Polo, and A. Massa, "Modular design of hexagonal phased arrays through diamond tiles," *IEEE Trans. Antennas Propag.*, vol.68, no. 5, pp. 3598-3612, May 2020.

[16] N. Anselmi, L. Poli, P. Rocca, and A. Massa, "Design of simplified array layouts for preliminary experimental testing and validation of large AESAs," *IEEE Trans. Antennas Propag.*, vol. 66, no. 12, pp. 6906-6920, Dec. 2018.

[17] N. Anselmi, P. Rocca, M. Salucci, and A. Massa, "Contiguous phase-clustering in multibeam-on-receive scanning arrays" *IEEE Trans. Antennas Propag.*, vol. 66, no. 11, pp. 5879-5891, Nov. 2018.

[18] N. Anselmi, P. Rocca, M. Salucci, and A. Massa, "Irregular phased array tiling by means of analytic schemata-driven optimization," *IEEE Trans. Antennas Propag.*, vol. 65, no. 9, pp. 4495-4510, Sept. 2017.

[19] N. Anselmi, P. Rocca, M. Salucci, and A. Massa, "Optimization of excitation tolerances for robust beamforming in linear arrays" *IET Microwaves, Antennas & Propagation*, vol. 10, no. 2, pp. 208-214, 2016.